

Matter and charge radius of ${}^6\text{He}$ in the hyperspherical-harmonics approach

S. Bacca,^{1,*} N. Barnea,^{2,†} and A. Schwenk^{3,4,‡}

¹*TRIUMF, 4004 Wesbrook Mall, Vancouver, BC, V6T 2A3, Canada*

²*Racah Institute of Physics, Hebrew University, 91904, Jerusalem, Israel*

³*ExtreMe Matter Institute EMMI, GSI Helmholtzzentrum für Schwerionenforschung GmbH, 64291 Darmstadt, Germany*

⁴*Institut für Kernphysik, Technische Universität Darmstadt, 64289 Darmstadt, Germany*

We present *ab-initio* calculations of the binding energy and radii of the two-neutron halo nucleus ${}^6\text{He}$ using two-body low-momentum interactions based on chiral effective field theory potentials. Calculations are performed via a hyperspherical harmonics expansion where the convergence is sped up introducing an effective interaction for non-local potentials. The latter is essential to reach a satisfactory convergence of the extended matter radius and of the point-proton radius. The dependence of the results on the resolution scale is studied. A correlation is found between the radii and the two-neutron separation energy. The importance of three-nucleon forces is pointed out comparing our results and previous calculations to experiment.

PACS numbers: 21.10.Dr, 21.10.Gv, 21.60.De, 27.20.+n

I. INTRODUCTION

The physics of strong interactions gives rise to fascinating phenomena like the formation of a halo structure where one or more loosely-bound nucleons surround a tightly bound core. The lightest known halo system is the ${}^6\text{He}$ nucleus, made of two neutrons and a ${}^4\text{He}$ core [1]. This nucleus is of Borromean nature, where the two-neutron and neutron-core subsystems are unbound, but the three-body system is held together [2]. ${}^6\text{He}$ is a radioactive nucleus that undergoes β -decay with a half-life of 0.8 s [3]. Despite this short life-time, a combination of nuclear and atomic physics techniques recently enabled a series of precision measurements of ${}^6\text{He}$. The ground-state energy has been measured directly for the first time at TITAN [4], leading to an improved value of its charge radius [5, 6]. Understanding and predicting these extreme phenomena presents a great testing ground for theory, leading to a deeper understanding of the strong force and nuclear interactions for neutron-rich systems. As a light nucleus, the study of ${}^6\text{He}$ is amenable to *ab-initio* methods starting from nuclear forces. The simultaneous description of the large radius and small binding of the halo neutrons makes the reproduction of the precise experimental data for halo nuclei particularly challenging.

One of the central advances in nuclear theory has been the development of chiral effective field theory (EFT) for nuclear forces [7, 8], rooted in quantum chromodynamics (QCD). In this formalism nucleon-nucleon (NN) interactions and many-body forces are constructed systematically and consistently. Before that, the traditional models to describe the interaction among nucleons were based on phenomenology or meson exchange theories. For light nuclei, *ab-initio* methods have established the quantita-

tive importance of three-nucleon (3N) forces for ground-state properties, excitations and reactions [9–12]. In addition, first approximate studies have shown new facets of 3N forces in heavier neutron-rich nuclei [13–15]. Despite these developments, 3N forces based on chiral EFT remain unexplored in halo nuclei.

In the literature, several *ab-initio* calculations of halo nuclei with traditional nucleon-nucleon (NN) potentials exist for both energy and radii, e.g., within the No-Core Shell Model (NCSM) with meson-exchange and phenomenological interactions [16], Fermionic Molecular Dynamics (FMD) studies based on the Unitary Correlation Operator Method (UCOM) potential [17], and the Microscopic Cluster Model (MCM) with semi-realistic interactions [18]. The only existing converged calculations that explicitly include 3N forces are based on the Green's Function Monte Carlo (GFMC) method [9]. While light nuclei have been investigated with chiral EFT potentials using the NCSM [11], there are no results for ${}^6\text{He}$ based on chiral NN and 3N interactions. The rapid Gaussian fall-off of the NCSM wave function does not make it the optimal method to investigate the extended halo nuclei. The correct description of the exponential fall-off can be achieved by combining the NCSM with the Resonating Group Method, as done in [19] for one-neutron halo nuclei.

In this paper, we present a chiral EFT based study of ${}^6\text{He}$, limited to two-body forces, as a first step towards predicting halo nuclei from EFT. Some of the results of this work have been presented in [4]. Here we give a complete overview of our theoretical study and explain the calculations in detail.

We combine the renormalization group (RG) evolution of chiral EFT potentials to low-momentum interactions [20] with the *ab-initio* Hyperspherical Harmonics (HH) method for ${}^6\text{He}$ [21]. Our work goes beyond the previous coupled-cluster theory investigation [22] of the helium isotopes in that we study the cutoff variation, as a tool to probe the effects of many-body forces on the binding energy and also on the radii of ${}^6\text{He}$. A similar

*E-mail: bacca@triumf.ca

†E-mail: nir@phys.huji.ac.il

‡E-mail: schwenk@physik.tu-darmstadt.de

study of the cutoff variation was performed in [23] using similarity-RG-evolved EFT potentials within the NCSM, where only binding energies were investigated within a limited Hilbert space ($N_{\text{max}} = 10$) for ${}^6\text{He}$. As opposed to a shell model expansion, the use of the hyperspherical basis enables to better describe the exponential fall-off of the nuclear wave function, which is important to provide precise results for ${}^6\text{He}$. This work also goes beyond our first study [24], since here we present converged results for the energy and new calculations of radii for ${}^6\text{He}$, where the use of the effective interaction method enables to speed up the convergence.

This paper is organized as follows. In Section II we describe the theoretical aspects of the interaction and of the few-body method. In Section III we present our results for the binding energy and radii of ${}^6\text{He}$, which are compared to the experimental data in Section IV. Finally, we conclude in Section V.

II. THEORETICAL ASPECTS

A. Nuclear forces

Nuclear forces depend on a resolution scale, which we denote by a generic momentum cutoff Λ , and the Hamiltonian consists of NN and corresponding many-body (3N, 4N, ...) interactions [7, 8]:

$$H(\Lambda) = T + V_{\text{NN}}(\Lambda) + V_{\text{3N}}(\Lambda) + V_{\text{4N}}(\Lambda) + \dots \quad (1)$$

For most nuclei, the typical momenta are of the order of the pion mass, $Q \sim m_\pi$, and therefore pion exchanges are included explicitly in nuclear forces. In chiral EFT [7, 8], nuclear interactions are organized in a systematic expansion in powers of Q/Λ_b , where Λ_b denotes the breakdown scale, roughly $\Lambda_b \sim m_\rho$. At a given order, this includes contributions from one- or multi-pion exchanges and from contact interactions, with short-range couplings that depend on the resolution scale Λ and for each Λ are fit to data. At N³LO [or $(Q/\Lambda_b)^4$], chiral NN interactions accurately reproduce low-energy NN scattering [7, 8].

In the current study we take the Entem and Machleidt N³LO chiral NN potential with $\Lambda = 500$ MeV [25] as a starting point, and then use the RG [20] to evolve it to low-momentum interactions $V_{\text{low } k}$ with $\Lambda = 1.8\text{--}2.4\text{ fm}^{-1}$ (360–480 MeV). To the evolved Hamiltonian, we add the Coulomb and other standard electromagnetic interactions. The RG preserves the long-range pion exchanges and includes subleading contact interactions, so that NN scattering data are reproduced. We use the RG to soften the short-range repulsion and short-range tensor components of the initial chiral interactions so that convergence of the few-body calculations is vastly accelerated. The cutoff variation of few- and many-body observables then serves as an estimate of the theoretical uncertainty due to neglected 3N and higher-body forces. The addition of evolved 3N forces, which is expected to

reduce the cutoff dependence, will be pursued in future work using the Similarity RG evolution in momentum space [26].

B. Hyperspherical-harmonics approach

Given the Hamiltonian H we use the HH expansion to solve the Schrödinger equation. The HH method, typically employed in few-body physics to study nuclei with mass number $A=3$ and 4, can be extended to the investigation of ${}^6\text{He}$ (see, e.g., [27, 28]), using a powerful antisymmetrization algorithm introduced in [21]. This approach is translationally invariant, being constructed with the Jacobi coordinates

$$\begin{aligned} \boldsymbol{\eta}_0 &= \frac{1}{\sqrt{A}} \sum_{i=1}^A \mathbf{r}_i, \\ \boldsymbol{\eta}_{k-1} &= \sqrt{\frac{k-1}{k}} \left(\mathbf{r}_k - \frac{1}{k-1} \sum_{i=1}^{k-1} \mathbf{r}_i \right), \quad k = 2, \dots, A, \end{aligned} \quad (2)$$

where \mathbf{r}_i are the particle coordinates. Using the $\boldsymbol{\eta}_i$ one can construct the hyperspherical coordinates composed of one hyperradial coordinate $\rho = \sqrt{\sum_{i=1}^{A-1} \boldsymbol{\eta}_i^2}$ and a set of $(3A-4)$ angles that we denote with Ω (for more details see [21]). In the HH method, the wave-function expansion reads

$$\Psi(\boldsymbol{\eta}_1, \dots, \boldsymbol{\eta}_{A-1}, s_1, \dots, s_A, t_1, \dots, t_A) = \sum_{[K]n}^{K_{\text{max}}, n_{\text{max}}} C_{[K]n} R_n(\rho) \mathcal{Y}_{[K]}(\Omega, s_1, \dots, s_A, t_1, \dots, t_A), \quad (3)$$

where s_i and t_i are the spin and isospin of nucleon i , respectively, $C_{[K]n}$ is the coefficient of the expansion, labeled by $[K]$, which represents a cumulative quantum number that includes the grandangular momentum K related to the hyperspherical harmonics $\mathcal{Y}_{[K]}$, and n labels the hyperradial wave function $R_n(\rho)$. The latter is given by

$$R_n(\rho) = \sqrt{\frac{n!}{(n+a)!}} b^{-\frac{3(A-1)}{2}} \left(\frac{\rho}{b}\right)^{\frac{a-(3A-4)}{2}} L_n^a\left(\frac{\rho}{b}\right) e^{-\rho/2b}, \quad (4)$$

where L_n^a are the generalized Laguerre polynomials, and b is a scale parameter. Equation (4) shows that the hyperradial basis functions fall-off exponentially as $-b/2\rho$. The Laguerre polynomials provide a power expansion in ρ/b which gives sufficient flexibility to describe the wave function in the short and intermediate range. As the wave-function expansion contains more and more hyperradial terms, i.e., Laguerre functions in Eq. (4), the correct hyperradial structure of the nuclear wave function is recovered regardless of the value of b . With about 40 hyperradial states, we observed a 0.05% relative change in the energy when b is varied by one order of magnitude.

Recently, we extended the use of the HH basis for non-local interactions [29, 30], by expanding the potential in harmonic-oscillator matrix elements. In [24] we used a HH expansion to study the energy of ${}^6\text{He}$ with $V_{\text{low } k}$ potentials. A rather slow convergence was observed, especially for the larger values of Λ , and we therefore performed an exponential extrapolation of the variational HH energies to the infinite Hilbert space. The same variational argument, however, cannot be used for other observables, like the radii. To further speed up the convergence of the calculation, we employed an effective interaction of the Lee-Suzuki type. This method, called Effective Interaction Hyperspherical Harmonics (EIHH), was first introduced in [31] and recently extended to non-local potentials in [32]. In the following, we present our results for the ground-state energies and radii which we obtained with the EIHH method using chiral low-momentum potentials.

III. RESULTS AND DISCUSSION

The main focus of this work is to study the ${}^6\text{He}$ nucleus. Nevertheless, we first consider ${}^4\text{He}$. This allows us to highlight the different convergence patterns between the HH and EIHH methods, as well as to benchmark our results with those of other few-body techniques.

In Fig. 1, we compare the convergence pattern of the HH to the EIHH approach for ${}^4\text{He}$. The ground-state energy and rms (root-mean-square) matter radius are presented as a function of the maximum grandangular momentum K_{max} used in the wave-function expansion. Larger spaces are accessible for ${}^4\text{He}$ but are not necessary for low-momentum interactions. The cutoff of the $V_{\text{low } k}$ chiral potential used in Fig. 1 is $\Lambda = 2.0 \text{ fm}^{-1}$, but a very similar convergence is obtained for cutoffs in the range $1.6 \leq \Lambda \leq 2.8 \text{ fm}^{-1}$. The energy is in agreement with the Faddeev-Yakubovsky result of $-28.65(5) \text{ MeV}$ [33] with the same potential. For the cutoff range $\Lambda = 1.8 - 2.4 \text{ fm}^{-1}$, the ${}^4\text{He}$ ground-state energy varies from $29.30 - 27.40 \text{ MeV}$ [24]. In addition, we remind the reader that if one uses the Entem and Machleidt N^3LO chiral NN potential [25], without evolving it to $V_{\text{low } k}$, the ${}^4\text{He}$ ground-state energy is -25.38 MeV [32]. The radius obtained with the EIHH has already been benchmarked with other few-body methods in [32] using the N^3LO chiral potential [25]. From Fig. 1 it is apparent that, even though an excellent convergence can be reached within the model space for both the HH and EIHH case, the EIHH convergence rate is superior, since with $K_{\text{max}} = 4$ one has already reached the converged value at a sub-percentage level. We also note that in case of the HH expansion, the radius converges slower than the energy. In fact, at $K_{\text{max}} = 8$ the radius is converged only within 0.15% whereas the energy is within 0.06%. In the same K_{max} space, the EIHH results are converged to 0.03% both for the energy and the radius.

We can now focus on the ${}^6\text{He}$ nucleus. In Fig. 2, we

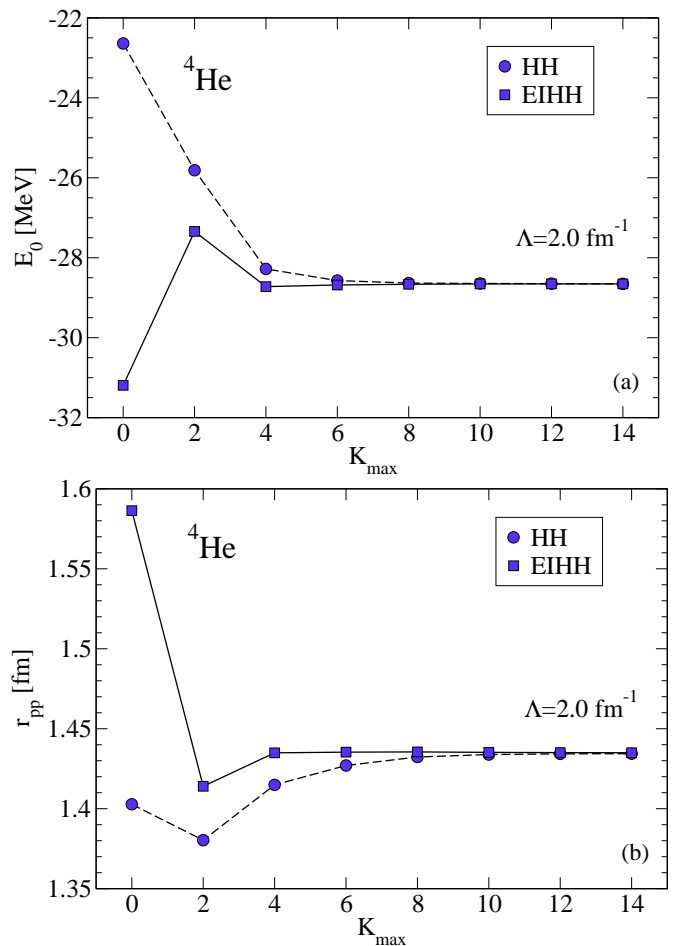


FIG. 1: (Color online) ${}^4\text{He}$ ground-state energy (upper panel) and rms matter radius (lower panel) as a function of the maximum grandangular momentum K_{max} used in the wave-function expansion. The convergence pattern of the HH (circles) expansion is compared to the EIHH (squares). The cutoff of the $V_{\text{low } k}$ chiral potential is $\Lambda = 2.0 \text{ fm}^{-1}$.

present the convergence patterns of the HH and EIHH methods for the ground-state energy as a function of the grandangular momentum K_{max} . The patterns are presented for three different cutoffs $\Lambda = 1.8, 2.0, 2.4 \text{ fm}^{-1}$ of the $V_{\text{low } k}$ chiral potential. The maximum value of K_{max} that we can reach with the present codes and computing capability for ${}^6\text{He}$ is 14, which corresponds to about 3×10^6 basis states. The cutoff range $\Lambda = 1.8 - 2.4 \text{ fm}^{-1}$ has been chosen to speed up the convergence of the basis expansion. When Λ increases, the result of the starting Entem and Machleidt potential [25] should be recovered. Converged results, especially for the radii, are however very hard to achieve within a $K_{\text{max}} = 14$ model space.

The HH results are taken from [24] and plotted together with the new EIHH results. The value obtained from the exponential extrapolation of the HH results with error bar obtained as explained in [24] is also shown. One can readily see that the convergence is faster when the lowest cutoff $\Lambda = 1.8 \text{ fm}^{-1}$ is used, because the inter-

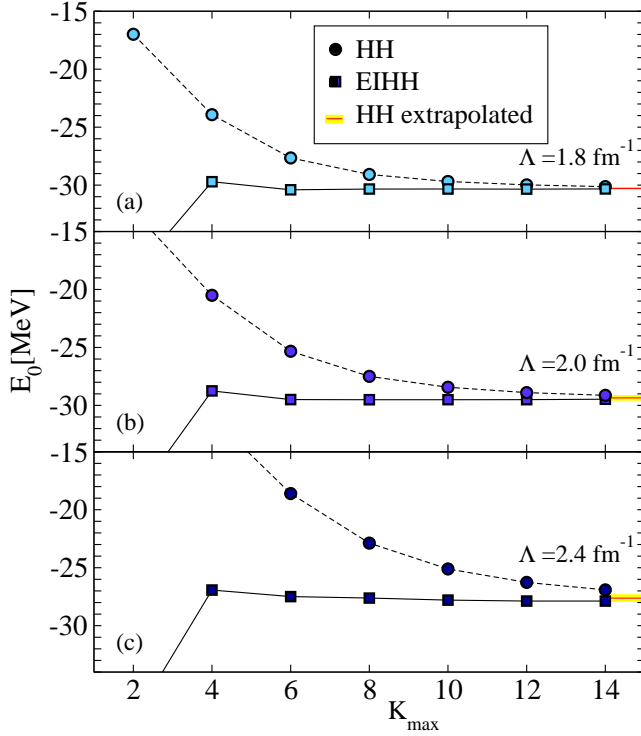


FIG. 2: (Color online) ${}^6\text{He}$ ground-state energies as a function of the grandangular momentum K_{max} obtained for three different values of the cutoff $\Lambda = 1.8, 2.0, 2.4 \text{ fm}^{-1}$ of the $V_{\text{low } k}$ chiral potential. The HH convergence pattern is taken from [24] and plotted together with the new EIH results. The value obtained from the exponential extrapolation of the HH results with the corresponding error bar (see [24]) is also shown.

action is softer. In this case, in fact, the curve for the HH expansion reaches the EIH one within the model space size of $K_{\text{max}} = 14$. For the larger cutoff values, and most evident for $\Lambda = 2.4 \text{ fm}^{-1}$ this is not the case, because the HH convergence is too slow to allow a satisfactory convergence within the accessible spaces. In [24] we extrapolated the variational HH results. It is reassuring that the HH extrapolated results agree with the EIH energies within the error bar for all the cutoffs used. Even though an extrapolation of the variational results is justifiable for ground-state energies, the use of the EIH approach enables one to avoid extrapolations. One can readily see in Fig. 2 that the convergence pattern of the EIH method is excellent, as proven by the nice flattening of the curve from $K_{\text{max}} = 4$. For this K_{max} space size and for the larger cutoff $\Lambda = 2.4 \text{ fm}^{-1}$ the HH result is still about 15 MeV above the converged value, whereas the EIH is within 3% of it.

We can now turn to the calculation of the radii. In case of a halo nucleus it is interesting to study both the rms matter radius and the rms point-proton radius or rms point-neutron radius. They are calculated as the expectation values of the operator $r_{\text{m/pp/pn}} =$

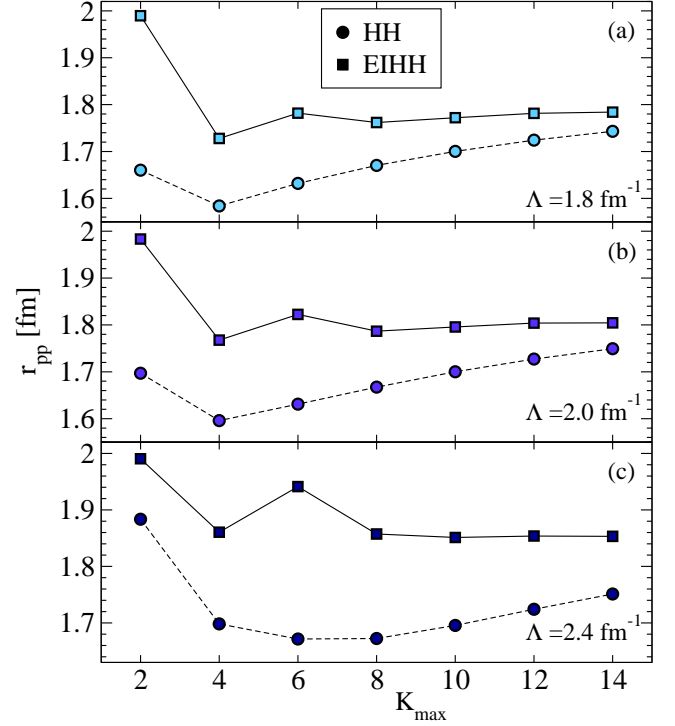


FIG. 3: (Color online) ${}^6\text{He}$ rms point-proton radius as a function of the grandangular momentum K_{max} obtained for three different values of the cutoff $\Lambda = 1.8, 2.0, 2.4 \text{ fm}^{-1}$ of the $V_{\text{low } k}$ chiral potential. The HH and EIH convergence patterns are compared.

$$\sqrt{\langle \psi_0 | r_{\text{m/pp/pn}}^2 | \psi_0 \rangle}, \text{ where}$$

$$\begin{aligned} r_{\text{m}}^2 &= \frac{1}{A} \sum_i^A (\mathbf{r}_i - \mathbf{R}_{\text{cm}})^2, \\ r_{\text{pp}}^2 &= \frac{1}{Z} \sum_i^A (\mathbf{r}_i - \mathbf{R}_{\text{cm}})^2 \left(\frac{1 + \tau_i^3}{2} \right), \\ r_{\text{pn}}^2 &= \frac{1}{N} \sum_i^A (\mathbf{r}_i - \mathbf{R}_{\text{cm}})^2 \left(\frac{1 - \tau_i^3}{2} \right), \end{aligned} \quad (5)$$

are the matter radius, the point-proton, and the point-neutron radius operators, respectively. Here $\mathbf{R}_{\text{cm}} = \frac{1}{\sqrt{A}} \boldsymbol{\eta}_0$ is the center-of-mass coordinate and τ_i^3 is the third component of the isospin of nucleon i .

In Fig. 3, the convergence patterns of the HH and EIH methods are shown for the case of the point-proton radius as a function of K_{max} . The three different values of the cutoff $\Lambda = 1.8, 2.0, 2.4 \text{ fm}^{-1}$ of the $V_{\text{low } k}$ chiral potential have been used. As already observed for ${}^4\text{He}$, one can see that the convergence of the HH method is slow for the radius. For ${}^6\text{He}$ it is so slow that convergence cannot be reached within the accessible K_{max} spaces. With the EIH method the convergence pattern is improved significantly and allows to provide solid result for this observable.

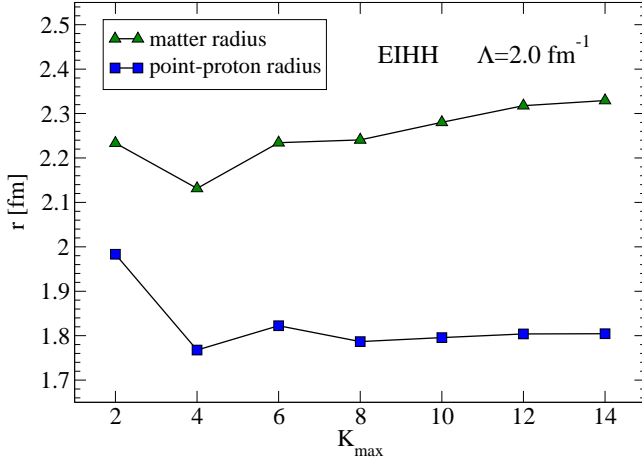


FIG. 4: (Color online) EIHH results of the ${}^6\text{He}$ matter radius and point-proton radius as a function of the grandangular momentum K_{max} obtained for a cutoff value $\Lambda = 2.0 \text{ fm}^{-1}$ of the $V_{\text{low } k}$ chiral potential.

TABLE I: ${}^4\text{He}$ point-proton radius and ${}^6\text{He}$ point-proton, point-neutron and matter radius for three different cutoffs $\Lambda = 1.8, 2.0, 2.4 \text{ fm}^{-1}$ obtained with the EIHH method. All radii are in fm. The two-neutron separation energy S_{2n} is shown as well in MeV.

$\Lambda [\text{fm}^{-1}]$	${}^4\text{He } r_{\text{pp}}$	${}^6\text{He } r_{\text{pp}}$	${}^6\text{He } r_{\text{pn}}$	${}^6\text{He } r_{\text{m}}$	${}^6\text{He } S_{2n}$
1.8	1.427(7)	1.78(1)	2.51(6)	2.30(6)	1.036(7)
2.0	1.435(7)	1.804(9)	2.54(6)	2.33(5)	0.82(4)
2.4	1.464(7)	1.853(9)	2.60(4)	2.39(3)	0.48(9)

In Fig. 4, we compare the convergence of the matter and point-proton radii for ${}^6\text{He}$ for a cutoff of $\Lambda = 2.0 \text{ fm}^{-1}$. The matter radius is about 30% larger than the point-proton radius due to the neutron halo. This is in agreement with the finding of other calculations, like the NCSM [16]. As a result of the halo, we also observe that the convergence of the matter radius is slower than that of the point-proton radius. In order to accurately describe the outer two halo neutrons, which contribute to the matter radius but not directly to the point-proton radius [except for a simple center-of-mass shift, see Eq. (5)], a larger space is required.

In Table I, we present our EIHH results for the point-proton, matter and point-neutron radii of ${}^6\text{He}$ for different cutoffs and compare it to the ${}^4\text{He}$ radii as a reference. As an estimate of the theoretical error associated with the few-body method we take the difference between the largest possible calculation ($K_{\text{max}} = 14$) and the $K_{\text{max}} = 10$ result, or minimally 0.5%.

As mentioned before the errors are larger for the matter and point-neutron radii than for the point-proton radius. For all three cutoffs studied, we find that the ${}^6\text{He}$ point-proton radius is larger than the ${}^4\text{He}$ point-proton radius by about 25-27%. Similar enhancements

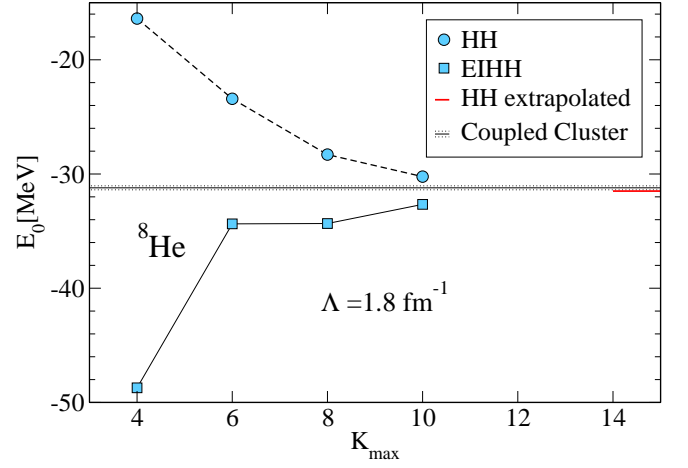


FIG. 5: (Color online) ${}^8\text{He}$ ground-state energy calculated with the EIHH and HH method as a function of the grandangular momentum K_{max} obtained for a cutoff of $\Lambda = 1.8 \text{ fm}^{-1}$ of the $V_{\text{low } k}$ chiral potential. The extrapolated HH results are shown as a reference and compared to the coupled cluster results from [24].

have been found within the NCSM [16] using different two-body potentials. The ${}^6\text{He } r_{\text{pp}}$ is larger than the ${}^4\text{He } r_{\text{pp}}$ because of two effects: recoil of the center-of-mass due to the presence of the halo neutrons in ${}^6\text{He}$ and core polarization. In our approach these two effects are both taken into account and cannot be separated. As shown in Table I, we find that the point-neutron radius is about 40% larger than the point-proton radius, similar to other calculations [16, 18].

Next, we discuss the cutoff dependence of our results with two-body interactions only. The cutoff variation of the energy and radii is significantly larger than the theoretical uncertainties due to the few-body method, which we have estimated above. The cutoff variation is due to neglected three-body and many-body interactions in the Hamiltonian $H(\Lambda)$. Varying the cutoff over the range $1.8 - 2.4 \text{ fm}^{-1}$ leads to a running of about 8% in the energy and of 4% in the radii. The latter are long-range observables, which are less sensitive to the Λ -dependence. Our results clearly highlight the fact that 3N forces are required for energies and radii.

We have also explored the four-neutron halo nucleus ${}^8\text{He}$ with the HH expansion. In Fig. 5, we show the ${}^8\text{He}$ ground-state energy from a $V_{\text{low } k}$ chiral potential with $\Lambda = 1.8 \text{ fm}^{-1}$. Convergence patterns are shown for the HH and EIHH methods as a function of the grandangular momentum K_{max} . We observe that the convergence of the calculations is very slow. With the present codes and computing capabilities we are not able to access larger K_{max} spaces, so that fully converged calculations cannot be provided at the moment. We have tried an exponential extrapolation of the HH results and present it as a reference in Fig. 5. We observe that the EIHH method seems to be less effective for ${}^8\text{He}$ than for ${}^6\text{He}$, because the second point in K_{max} is still a few MeV away from

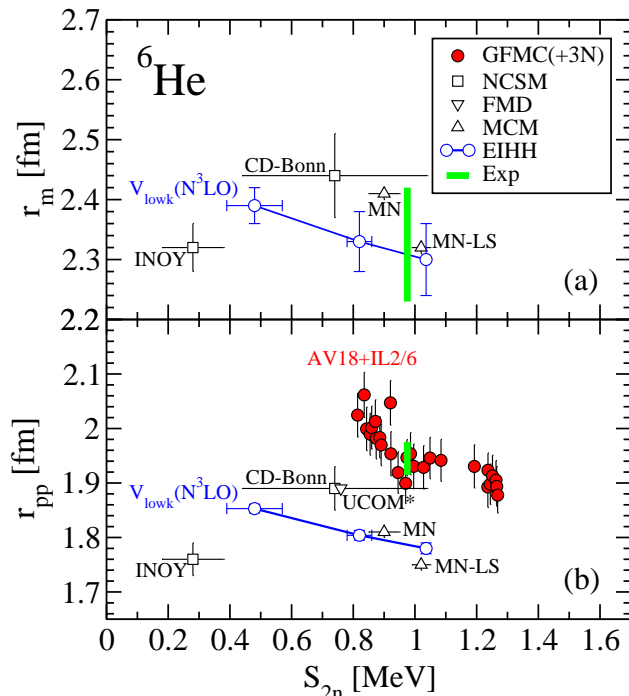


FIG. 6: Correlation plot of the ${}^6\text{He}$ matter radius (upper panel) and point-proton radius (lower panel) versus two-neutron separation energy S_{2n} . The experimental range, shown by the bar (see text for details), is compared to theory based on different methods (NCSM [16], FMD [17], MCM [18] and our EIHH results using different NN interactions only and including 3N forces fit to light nuclei (only for GFMC [9])). Calculational error bars are shown when available.

the reference of the extrapolation. It is interesting to note that, even if not very accurate, the extrapolated HH lies close to the coupled-cluster result obtained in [24] where singles and doubles excitations plus approximated triples were taken into account. As error for the latter we take 10% of the difference with respect to the Hartree-Fock calculation with the same potential, shown in Fig. 5 by the dotted line.

A. Comparison with experiment

Next, we compare our results to the available experimental data and to other *ab-initio* calculations.

The matter radius can be obtained from ion-scattering experiments, which however is considerably uncertain. We include three different data: in [34] r_m was measured from a combined analysis of the interaction cross section of ${}^6\text{He}$ with a carbon target and two-neutron removal cross sections of ${}^6\text{He}$ projectiles, leading to 2.33 ± 0.04 fm; in [35] and [36] r_m was measured from proton elastic scattering in inverse kinematics leading to 2.30 ± 0.07 fm and 2.37 ± 0.05 fm, respectively. In Fig. 6(a) we present these data as a (green) band, which spans the three values

with their associated error bars.

The charge radius r_{ch} of halo nuclei, instead, can be precisely and accurately measured via laser spectroscopy techniques [5, 6]. The extraction of r_{ch} from measured isotopic shifts requires very precise mass measurements and atomic theory calculations. The ${}^6\text{He}$ charge radius has been recently reevaluated using input from the first direct mass measurement of this halo nucleus, leading to $r_{ch} = 2.060 \pm 0.008$ fm [4]. In order to compare the experimental charge radius with theory, we convert it into a point-proton radius r_{pp} using [37]:

$$r_{pp}^2 = r_{ch}^2 - R_p^2 - (N/Z) \cdot R_n^2 - 3/(4M_p^2) - r_{so}^2, \quad (6)$$

where R_p^2 and $R_n^2 = -0.1161(22)$ fm² are the proton and neutron mean-square charge radii, respectively, $3/(4M_p^2) = 0.033$ fm² is a first-order relativistic (Darwin-Foldy) correction [38] and r_{so}^2 is a spin-orbit nuclear charge-density correction. The latter should be calculated from *ab-initio* wave functions and we will discuss our results later. Because such a calculation is not available for all methods, we prefer to use a common estimate for r_{so}^2 in the conversion of the experimental charge radius to r_{pp}^2 . In [37], the spin-orbit correction was estimated to be -0.08 fm² in the case of pure $p_{3/2}$ halo neutrons for ${}^6\text{He}$. We conservatively took 0.08 fm² as the corresponding error. For R_p the Review of Particle Physics [39] value is $0.877(7)$ fm. Recently, R_p has been also precisely measured from spectroscopy of muonic hydrogen [40] leading to $0.84184(67)$ fm. Using these two values for R_p with the above mentioned spin-orbit corrections in Eq. (6) we obtain $r_{pp} = 1.938 \pm 0.023$ fm and 1.953 ± 0.022 fm for ${}^6\text{He}$, respectively. The experimental (green) band in Fig. 6(b) includes both values with their errors.

In order to present a combined comparison of our results to experiment we show plots of the matter radius r_m and point-proton r_{pp} radius versus the two-neutron separation energy S_{2n} . The cutoff dependence of our EIHH results based on V_{lowk} chiral potentials allows us to study the correlation between these observables, as shown in Fig. 6. We observe that both the matter radius, in panel (a), and the point-proton radius, in panel (b), increase when the separation energy decreases. A smaller separation energy leads to a more extended halo structure and thus larger r_m and r_{pp} . Even though not unexpected, it is interesting to see that such a correlation is obtained from a set of phase-shift-equivalent interactions. The lower separation energy and larger radii are found for $\Lambda = 2.4$ fm⁻¹. This indicates that for larger cutoff values the ${}^6\text{He}$ nucleus is unbound, as is the case with the Argonne v_{18} (AV18) potential [41].

The correlation band obtained from the EIHH results goes through the experimental range for r_m , which has a large uncertainty, but does not go through the experimental range for r_{pp} . Due to the smaller uncertainty, this poses a stronger test for theory. Before discussing more the comparison between theory and experiment, we

also show the results of other *ab-initio* calculations. The GFMC energies [9] are the only existing converged calculations with 3N forces. Here, the employed phenomenological potentials are constrained to reproduce the properties of light nuclei, including ${}^6\text{He}$. In [9] it is explained that the GFMC method does not reproduce the radii of halo nuclei as precisely as energies and spectra of light nuclei, hence the different points in Fig. 6(b). The scatter in Fig. 6(b) gives some measure of the uncertainty in the GFMC method as well as an uncertainty in the 3N force models used [the IL2 and IL6 three-body forces were used with the AV18 NN potential] [9].

Calculations with NN forces only include the FMD results based on the UCOM potential plus a phenomenological correction to account for three-body physics (which we denote with UCOM*) [17], the NCSM results based on the CD-Bonn and INOY potentials [16], and variational MCM results based on the Minnesota (MN) and MN with spin-orbit (MN-LS) potentials [18]. Figure 6 shows that all theoretical results based on NN forces only are compatible with the large experimental range for r_m , but not with r_{pp} . They consistently lie at lower S_{2n} and smaller r_{pp} values. The comparison to theory in Fig. 6(b) clearly highlights the importance of including 3N forces. Figure 6 also shows the importance of comparing theoretical predictions to more than one observable. To illustrate this, both NCSM (using CD-Bonn) and the GFMC results show a good agreement for the point-proton radius, while the NCSM result has a large error for S_{2n} and tends to underpredict the two-neutron separation energy.

The observation that the $r_{pp} - S_{2n}$ correlation band shown by the EIH method does not go through experiment is similar to the Phillips and Tjon lines in few-body systems [42], when only NN interactions are included. Three-body physics manifests itself as a breaking from this line/band. This behavior is also supported by the variational MCM results.

Finally, we discuss the spin-orbit radius. The r_{so}^2 term is a leading-order relativistic correction to the charge radius and should be calculated from consistent *ab-initio* wave functions. Following [43] and deriving the form of the r_{so}^2 operator from the relativistic spin-orbit correction to the charge density, we obtain

$$r_{so}^2 = \frac{1}{Z} \sum_i \frac{2\mu_i - e_i}{2m^2} \boldsymbol{\sigma}_i \cdot \boldsymbol{\ell}'_i, \quad (7)$$

where m , μ_i and e_i are the nucleon mass, magnetic moment and charge, respectively. Here, $\boldsymbol{\sigma}_i = 2\mathbf{s}_i$ and $\boldsymbol{\ell}'_i$ represents the nucleon angular momentum in the center-of-mass frame, defined as

$$\boldsymbol{\ell}'_i = (\mathbf{r}_i - \mathbf{R}_{cm}) \times \left(\mathbf{p}_i - \frac{1}{A} \mathbf{P}_{cm} \right). \quad (8)$$

The estimate for the spin-orbit correction from a shell-model picture based on pure $p_{3/2}$ halo neutrons is -0.08 fm^2 [37]. A microscopic calculation based on the Minnesota potential gives -0.0718 fm^2 [44].

TABLE II: ${}^6\text{He}$ spin-orbit relativistic correction to the point-proton radius for the different cutoffs $\Lambda = 1.8, 2.0, 2.4 \text{ fm}^{-1}$ obtained from the EIH method with $K_{\max} = 10$.

$\Lambda \text{ [fm}^{-1}\text{]}$	${}^6\text{He } \langle r_{so}^2 \rangle \text{ [fm}^2\text{]}$
1.8	-0.0828
2.0	-0.0822
2.4	-0.0808

Using a harmonic-oscillator potential and $K_{\max} = 2$ in the HH expansion we can numerically reproduce the analytical results of [37], if we correct for the center-of-mass as explained below. Working with antisymmetrized wave functions, one has $\langle \psi_0 | \sum_i O_i | \psi_0 \rangle = A \langle \psi_0 | O_A | \psi_0 \rangle$. For the operator in Eq. (7), one has to consider the spin-orbit term $\boldsymbol{\sigma}_A \cdot \boldsymbol{\ell}'_A$. In a shell-model picture one usually works in the lab system so that the operator $\boldsymbol{\ell}'_A$ is replaced with $\boldsymbol{\ell}_A = \mathbf{r}_A \times \mathbf{p}_A$. To see how $\boldsymbol{\ell}_A$ and $\boldsymbol{\ell}'_A$ are related, recall that in the coordinate system of Eq. (2) the following holds

$$\mathbf{r}_A = \sqrt{\frac{A-1}{A}} \boldsymbol{\eta}_{A-1} + \frac{1}{\sqrt{A}} \boldsymbol{\eta}_0, \quad (9)$$

$$\mathbf{p}_A = \sqrt{\frac{A-1}{A}} \mathbf{q}_{A-1} + \frac{1}{\sqrt{A}} \mathbf{q}_0, \quad (10)$$

where \mathbf{q}_{A-1} and \mathbf{q}_0 are the conjugate coordinates of $\boldsymbol{\eta}_{A-1}$ and $\boldsymbol{\eta}_0$, respectively. Taking the nucleus to be at rest, $\mathbf{q}_0 = 0$, one has

$$\boldsymbol{\ell}_A = \frac{A-1}{A} \boldsymbol{\ell}'_{\eta_{A-1}} + \sqrt{\frac{A-1}{A^3}} \boldsymbol{\eta}_0 \times \mathbf{q}_{A-1}, \quad (11)$$

where it can be shown that $\boldsymbol{\ell}_{\eta_{A-1}} = \boldsymbol{\eta}_{A-1} \times \mathbf{q}_{A-1} = \boldsymbol{\ell}'_A$. Assuming that the wave function factorizes in spherically symmetric center-of-mass and intrinsic components, the term $\langle \phi_{cm} | \boldsymbol{\eta}_0 | \phi_{cm} \rangle = 0$, so that

$$\boldsymbol{\ell}'_A = \frac{A}{A-1} \boldsymbol{\ell}_A. \quad (12)$$

Thus, in comparing to [37] a factor of $6/5$ for ${}^6\text{He}$ should be included when intrinsic operators are used, leading to $\langle r_{so}^2 \rangle = -0.096 \text{ fm}^2$. In Table II, we give results for $\langle r_{so}^2 \rangle = \langle \psi_0 | r_{so}^2 | \psi_0 \rangle$ obtained with the EIH method for the three different low-momentum potentials employed. Calculations have been performed up to $K_{\max} = 10$ which are converged at the few percent level. Our calculations deviate about 15% from the pure $p_{3/2}$ halo-neutrons estimate.

We observe that the spin-orbit correction to the radius is small and not enough to reconcile theory with experiment at the NN forces level. When used in Eq. (6) to convert the experimental charge radius to a point-proton radius, it leads to an enhancement of r_{pp} , going in the opposite direction with respect to what is needed to improve the agreement with experiment.

IV. CONCLUSIONS

We have carried out *ab-initio* calculations of the energy and radii of ${}^6\text{He}$, using two-body $V_{\text{low } k}$ interactions for different cutoffs based on a chiral EFT potential [25]. This work is part of an ongoing effort to utilizing chiral EFT to predict the properties of halo nuclei. The calculations were performed using the EHH method. The EHH ground-state energies are in agreement with previously published values obtained from extrapolating HH results. The effective interaction greatly improves the convergence of the radii of ${}^6\text{He}$, allowing us to avoid extrapolations. The neutron halo of ${}^6\text{He}$ manifests itself via a 30% (40%) enhancement of the matter radius (point-neutron radius) with respect to the point-proton radius.

In comparing with experiment, we have presented plots of the radii versus the two-neutron separation energy. We observe a correlation between radii and S_{2n} using the set of phase-shift-equivalent NN potentials obtained by varying the resolution scale. The correlation band overlaps with the experimental data only for the matter radius, which is relatively uncertain. For the accurately measured charge radius and inferred value of the point-proton radius, our results lie at too low r_{pp} and S_{2n} with respect to experiment. This is a general trend for

ab-initio results from NN interactions only. We have investigated whether the spin-orbit relativistic correction to the radius, needed for the comparison between theory and experiment, has an effect. From our calculations we observe that this correction is small and not enough to reconcile the differences with experiment at the NN forces level. Comparing our results to experiment and to the other *ab-initio* calculations it is evident that 3N forces are crucial. Efforts to include chiral 3N forces in our calculations are under way.

V. ACKNOWLEDGMENT

We thank M. Brodeur and J. Dilling for discussions. This work was supported in part by the Natural Sciences and Engineering Research Council (NSERC) and the National Research Council (NRC) of Canada, the Israel Science Foundation (Grant No. 954/09), the Helmholtz Alliance Program of the Helmholtz Association, contract HA216/EMMI “Extremes of Density and Temperature: Cosmic Matter in the Laboratory”, and the DFG through grant SFB 634. Numerical calculations were performed at TRIUMF.

-
- [1] I. Tanihata, J. Phys. G **22**, 157 (1996).
 - [2] B. Jonson, Phys. Rep. **389**, 1 (2004).
 - [3] A. Knecht *et al.*, Phys. Rev. Lett. **108**, 122502 (2012).
 - [4] M. Brodeur *et al.*, Phys. Rev. Lett. **108**, 052504 (2012).
 - [5] L. B. Wang *et al.*, Phys. Rev. Lett. **93**, 142501 (2004).
 - [6] P. Mueller *et al.*, Phys. Rev. Lett. **99**, 252501 (2007).
 - [7] E. Epelbaum, H.-W. Hammer and U.-G. Meißner, Rev. Mod. Phys. **81**, 1773 (2009).
 - [8] D. R. Entem and R. Machleidt, Phys. Rept. **503**, 1 (2011).
 - [9] S. C. Pieper, Riv. Nuovo Cim. **31**, 709 (2008).
 - [10] K. M. Nollett, S. C. Pieper, R. B. Wiringa, J. Carlson and G. M. Hale, Phys. Rev. Lett. **99**, 022502 (2007).
 - [11] P. Navrátil, S. Quaglioni, I. Stetcu and B. R. Barrett, J. Phys. G **36**, 083101 (2009).
 - [12] S. Bacca, N. Barnea, W. Leidemann and G. Orlandini, Phys. Rev. Lett. **102**, 162501 (2009).
 - [13] T. Otsuka, T. Suzuki, J. D. Holt, A. Schwenk and Y. Akaishi, Phys. Rev. Lett. **105**, 032501 (2010).
 - [14] J. D. Holt, T. Otsuka, A. Schwenk and T. Suzuki, J. Phys. G **39**, 085111 (2012).
 - [15] J. D. Holt, J. Menendez and A. Schwenk, arXiv:1108.2680.
 - [16] E. Caurier and P. Navrátil, Phys. Rev. C **73**, 021302(R) (2006).
 - [17] T. Neff and H. Feldmeier, Nucl. Phys. A **738**, 357 (2004).
 - [18] I. Brida and F. M. Nunes, Nucl. Phys. A **847**, 1 (2010).
 - [19] S. Quaglioni and P. Navrátil, Phys. Rev. C **79**, 044606 (2009).
 - [20] S. K. Bogner, R. J. Furnstahl and A. Schwenk, Prog. Part. Nucl. Phys. **65**, 94 (2010); S. K. Bogner, R. J. Furnstahl, S. Ramanan and A. Schwenk, Nucl. Phys. A **784**, 79 (2007).
 - [21] N. Barnea and A. Novoselsky, Phys. Rev. A **57**, 48 (1998); Ann. Phys. (N.Y.) **256**, 192 (1997).
 - [22] G. Hagen, D. J. Dean, M. Hjorth-Jensen and T. Papenbrock, Phys. Lett. B **656**, 169 (2007).
 - [23] S. K. Bogner, R. J. Furnstahl, P. Maris, R. J. Perry, A. Schwenk and J. P. Vary, Nucl. Phys. A **801**, 21 (2008).
 - [24] S. Bacca, A. Schwenk, G. Hagen and T. Papenbrock, Eur. Phys. J. A **42**, 553 (2009).
 - [25] D. R. Entem and R. Machleidt, Phys. Rev. C **68**, 041001(R) (2003).
 - [26] K. Hebeler, Phys. Rev. C **85**, 021002(R) (2012).
 - [27] S. Bacca, M. A. Marchisio, N. Barnea, W. Leidemann and G. Orlandini, Phys. Rev. Lett. **89**, 052502 (2002).
 - [28] S. Bacca, N. Barnea, W. Leidemann and G. Orlandini, Phys. Rev. C **69**, 057001 (2004).
 - [29] N. Barnea, W. Leidemann and G. Orlandini, Phys. Rev. C **74**, 034003 (2006).
 - [30] S. Bacca, Phys. Rev. C **75**, 044001 (2007).
 - [31] N. Barnea, W. Leidemann and G. Orlandini, Phys. Rev. C **61**, 054001 (2000); Nucl. Phys. A **693**, 565 (2001).
 - [32] N. Barnea, W. Leidemann and G. Orlandini, Phys. Rev. C **81**, 064001 (2010).
 - [33] A. Nogga, private communication.
 - [34] I. Tanihata, D. Hirata, T. Kobayashi, S. Shimomura, K. Sugimoto and H. Toki, Phys. Lett. B **289**, 261 (1992).
 - [35] G. D. Alkhazov, *et al.*, Phys. Rev. Lett. **78**, 2313 (1997).
 - [36] O. A. Kislev, *et al.*, Eur. Phys. J. A **25**, 215 (2005).
 - [37] A. Ong, J. C. Berengut and V. V. Flambaum, Phys. Rev. C **82**, 014320 (2010).
 - [38] J. L. Friar, J. Martorell and D. W. L. Sprung, Phys. Rev. A **56**, 4579 (1997).

- [39] K. Nakamura *et al.* (Particle Data Group), J. Phys. G **37**, 075021 (2010).
- [40] R. Pohl *et al.*, Nature **466**, 213 (2010).
- [41] S. C. Pieper, R. B. Wiringa and J. Carlson, Phys. Rev. C **70**, 054325 (2004).
- [42] P. F. Bedaque and U. van Kolck, Annu. Rev. Nucl. Part. Sci. **52**, 339 (2002).
- [43] J. L. Friar and J. W. Negele, Adv. Nucl. Phys. **8**, 219 (1975).
- [44] G. Papadimitriou, A. T. Kruppa, N. Michel, W. Nazarewicz, M. Płoszajczak and J. Rotureau, Phys. Rev. C **84**, 051304 (2011).